Improved thermal relaxation method for the simultaneous measurement of the specific heat and thermal conductivity

L. Demkó[1,a], I. Kézsmárki[1], M. Csontos[1,2], S. Bordács[1], and G. Mihály[1]

[1] Condensed Matter Research Group of the Hungarian Academy of Sciences and Department of Physics, Budapest University of Technology and Economics, 1111 Budapest, Hungary
[2] Solid State Physics Laboratory, ETH Zurich, 8093 Zurich, Switzerland

Abstract. A novel method for the simultaneous, high-resolution measurement of the specific heat c and the thermal conductivity κ is presented. A new experimental setup has been developed with special emphasis on the elimination of systematic errors arising from radiative heat loss. A self-consistent data evaluation method is implemented which takes the effects of the sample geometry on c and κ properly into account. The measurements were performed over a broad temperature regime from 3 K up to room temperature on three compounds from the family of strongly correlated electron systems. The differences in their thermal properties and their highly sample-dependent sizes and shapes demonstrate the extended scope of the proposed method.

1 Introduction

Simultaneous measurement of thermal conductivity and specific heat can reveal complementary information about the lattice and electronic properties and hence it is an efficient tool to study the physics of solids. Furthermore, parallel measurement of these thermal properties is useful to eliminate systematic errors arising from the difference between samples used in the individual measurements and from the possible changes in the experimental conditions. On the basis of thermal transport data, one can identify the heat carriers – such as electrons, phonons, magnons, etc. – and characterize their scattering mechanism. On the other hand, the measurement of specific heat is an adequate method to study the electronic density of states at the Fermi energy in metals, to determine the Debye temperature of the phonon system and to investigate the nature and the strength of electron-electron interaction in solids. In particular, the latter has been extensively used in a broad class of strongly correlated electron systems and played a crucial role in the study of heavy fermion compounds [1,2] as well as of the gap anisotropy in d-wave superconductors [3,4]. Thermal properties are also of general importance when studying anomalies associated with phase transitions in order to specify the order of the transition and whether it is characteristic of the bulk of the material or caused by a minority secondary phase.

In the present article we describe a flexible experimental approach, which is an improved version of the thermal relaxation method proposed by Kwok et al. [5] for the simultaneous measurement of the thermal conductivity and specific heat. By taking the effect of radiative heat loss into account, the new method extends the range of applicability to high temperatures (up to room temperature and above) for single crystals with any shape. We have tested the efficiency of the developed experimental setup by focusing on anomalies in the specific heat and thermal conductivity upon phase transitions of various kinds. Our results on tiny single crystals of three different compounds clearly demonstrate the accuracy of the new technique and its high sensitivity being able to capture even very small anomalies in the temperature dependence of either of the two quantities. Additionally, one can give a rough estimation for the sample emissivity based on the results obtained by the present method.

The structure of the paper is organized as follows. Section 2 gives an overview about the experimental setup followed by a detailed description of the methodology. In the latter, we give a numerical scheme for the high-accuracy determination of the thermal conductivity and specific heat in the presence of radiative heat loss inevitable in these experiments. New concepts to reduce the uncertainty in the absolute value of both quantities – mainly originating from the irregular and ill-defined shape of the available crystals – and to evaluate the sample's emissivity are also presented. Section 3 contains our results obtained on high-quality single crystals of $BaVS_3$, $2H$-$TaSe_2$ and κ-$(ET)_2Cu_2(CN)_3$ in comparison with corresponding data available in the literature. Both the sample geometry and the temperature regime of interest vary among these samples demonstrating the flexibility of the method. The $BaVS_3$ sample is rod-shaped with the dimensions of $8 \times 0.5 \times 0.5$ mm^3. We found that the effect of radiative heat loss is strong, ∼25% at room temperature due to its

---

[a] e-mail: `ldemko@dept.phy.bme.hu`

large S/A surface aspect ratio (surface area over cross section) which was previously pointed out in case of carbon nanotube bundles [6]. $2H$-TaSe$_2$ and κ-(ET)$_2$Cu$_2$(CN)$_3$ crystals have smaller surface aspect ratios corresponding to their planar shape with approximate dimensions of $4 \times 3 \times 0.4$ mm^3 and $2 \times 1.5 \times 0.15$ mm^3, respectively.

2 Experimental setup

Among the broad variety of the experimental methods [7–11] developed for the measurement of thermal conductivity and specific heat, we started from the so-called thermal relaxation method [5,12]. We improved this method by taking the effect of radiative heat loss into account in a fully quantitative manner. For the elimination of radiative heat loss of the sample in the course of steady-state measurement of thermal conductivity, Kwok et al. [5] described a procedure to match the temperature profile of the radiation shield to the one of the mounted sample by careful control of the heat fluxes. While this method can be successfully applied for large crystals with needle-like shape, it seems to be problematic for small samples with arbitrary shape. Furthermore, their algorithm is not capable for the parallel measurement of thermal conductivity and specific heat due to the incompatible time-scales of the long-term thermal matching and the fine resolution monitoring of the fast changes in the sample temperature during the relaxation process.

A schematic drawing of our experimental arrangement is shown in Figure 1. Here the specimen itself is used as the heat link between the heater and the base temperature of the sample holder. Because of the small sample size (maximum a few millimeter in length), we use differential thermocouples to monitor the temperature relative to the base temperature T_0 at the hot and cold ends (Fig. 1a) and an additional one in the middle of the sample (Fig. 1b). Chromel-constantan thermocouples are applicable over a broad range of temperature from $\sim$3 K up to 1140 K. The relative magnitude of the systematic errors arising from the convecting heat loss through the thermocouple wires can be kept below $\sim 10^{-5}$ by preparing spirals of the thin ($\lesssim 20$ μm) thermocouple wires. Tiny parts of commercial ceramic resistors with typical resistance of $\sim$10 kΩ are used as heaters contacted by similar spiraled wiring. It is also ensured that the heat capacity of the specimens are usually much larger than the total heat capacity of the heater (typically 1000:1). In order to minimize convecting heat loss along the sample, the sample chamber is evacuated down to $<10^{-5}$ mbar. To avoid an additional thermal voltage drop along the wires the end of each thermocouple wire is thermalized to a common heat trap of T_0 temperature.

2.1 Numerical model

In the absence of convection and radiative heat losses, the steady-state heat flow through a one-dimensional specimen has the following form in the frame of the linear response theory:

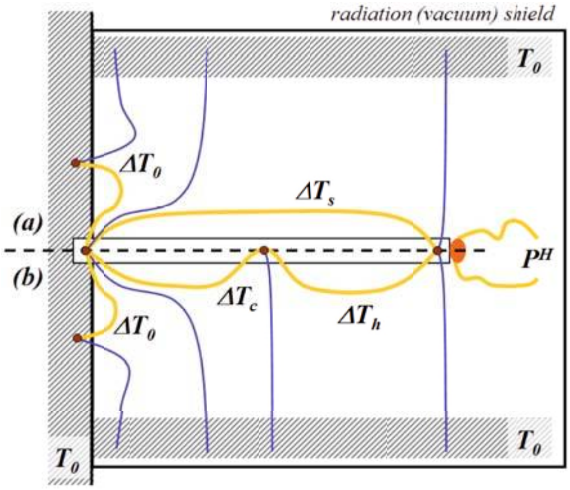

Fig. 1. (Color online) Schematic drawing of the sample chamber. One end of the sample is attached to the base plate of T_0 temperature while the heater is placed on its other end. Here P^H denotes the power dissipated by the heater. Thermocouples are fixed to the sample using silver paste with thin mylar foil in between for electrical isolation. Thick light color wires correspond to chromel while thin dark ones are constantan. The former is also used for the heater wiring. ΔT_s labels the temperature drop along the whole sample, while $\Delta T_c/\Delta T_h$ is the temperature difference between the cold/hot end and the middle of the sample, respectively. Note that ΔT_0 is normally zero, i.e. the cold end of the sample has strong heat link to the base plate. Upper part: standard arrangement for measuring the temperature at the hot and cold ends of the sample relative to the T$_0$ base temperature of the sample holder. Lower part: improved arrangement for mapping the temperature profile along the sample for facilitating geometrical corrections (see Sect. 2.4 for details).

$$j_Q = -\kappa \frac{\partial T}{\partial x},$$

where j_Q is the heat current density driven by the temperature gradient $\partial T/\partial x$ and κ is the thermal conductivity. The one-dimensional form of the continuity principle reads as

$$\frac{\partial Q}{\partial t} + \frac{\partial j_Q}{\partial x} = P(x),$$

where $P(x)$ is the heating power density introduced at position x. The $\partial Q/\partial t$ derivative of the heat density (also a function of the position) can be expressed as

$$\frac{\partial Q}{\partial t} = \frac{c}{v} \frac{\partial T}{\partial t},$$

with the c molar specific heat and v molar volume.

Analytical treatment of this problem is non-trivial due to the singularity in the gradient of the heat flow at the heater-sample connection. Thus, we used a numerical approach for the quantitative analysis and constructed a one-dimensional model similar to the one proposed previously by Kwok et al. [5] for the non-radiative case. We divide the sample into $N+1$ equal segments, where the index 0 labels the segment attached to the base plate of the sample holder while the last segment N is connected to the heater. We assume that the temperature is uniform inside the individual segments. Therefore, in this discrete model the actual temperature T_i depends only on the segment number ranging from $i = 0$ to N, where T_0 is the temperature of the first segment (cold end of the sample). In the following we assume, that due to the strong heat link between the cold end of the sample and the base plate, T_0 is equal to the base temperature of the sample holder.

After discretization the continuity principle applied to the segments can be written in the form of

$$c\frac{\rho AL}{MN}\dot{T}_i = \kappa\frac{AN}{L}(T_{i+1} - 2T_i + T_{i-1})$$

for $i = 1 \ldots N-1$, and

$$c\frac{\rho AL}{MN}\dot{T}_N = \kappa\frac{AN}{L}(-T_N + T_{N-1}) + P^H,$$

where M denotes the molar weight and ρ the mass density of the specimen with length of L and perpendicular cross section A. P^H is the power dissipated by the heater attached to the last segment (see Fig. 1 for correspondence). In a steady-state $\dot{T}_i \equiv 0$, thus the temperature values of the individual segments relative to the base temperature can be obtained by

$$\Delta T_i \equiv T_i - T_0 = \Delta T_s - (N-i)\frac{1}{\kappa}\frac{L}{AN}P^H,$$

where $\Delta T_s = T_N - T_0$ is the total temperature drop along the sample. The condition $\Delta T_0 \equiv 0$ directly results in the well-known relation for the heat conductivity coefficient $\kappa_0 = P^H L/\Delta T_s A$.

2.2 Effect of the radiative heat transfer

At high temperatures the radiative heat loss usually strongly affects the measurement of the thermal properties, especially for thin specimens due to their large surface aspect ratios. Considering thermal radiation from the sample surface and assuming that the environment (base plate and radiation shield) around the specimen has a uniform T_0 temperature, the heat loss caused by the radiation of the individual segments is given by

$$P_i^R = -\sigma S_i(\epsilon_s T_i^4 - \epsilon_0 T_0^4),$$

where ϵ_s and ϵ_0 are the surface emissivity of the specimen and of the surrounding sample holder, respectively, σ denotes the Stefan-Boltzmann constant while S_i is the outer surface area of the segments. Adding this term to the continuity principle leads to the following set of non-linear equations:

$$2c\dot{T}_i = \kappa\frac{MN^2}{\rho L^2}(T_{i+1} - 2T_i + T_{i-1}) - \sigma\frac{Mp}{\rho A}(\epsilon_s T_i^4 - \epsilon_0 T_0^4) \quad (1)$$

for $i = 1 \ldots N-1$, and

$$c\dot{T}_N = \kappa\frac{MN^2}{\rho L^2}(-T_N + T_{N-1}) - \sigma\frac{Mp}{\rho A}(\epsilon_s T_N^4 - \epsilon_0 T_0^4) + \frac{MN}{\rho AL}P^H, \quad (2)$$

where p is the perimeter of the perpendicular cross section. In this case, steady-state temperature gradients can be calculated according to

$$\Delta T_i = \Delta T_s + \frac{\sigma}{\kappa}\frac{pL^2}{AN^2}\sum_{j=1}^{N-i} j(\epsilon_s T_i^4 - \epsilon_0 T_0^4) - (N-i)\frac{1}{\kappa}\frac{L}{AN}P^H. \quad (3)$$

With the initial value κ_0 for the thermal conductivity, ΔT_N, $\Delta T_{N-1} \ldots \Delta T_0$ can be calculated recursively. The real value of the thermal conductivity can be iteratively approached by stressing the $\Delta T_0 \to 0$ self-consistency criterion, i.e., the value of κ in a certain step of the iteration is changed according to the value obtained for ΔT_0 in the same step. Note that the input parameters from the experiment are ΔT_s, P^H and the factors describing the sample geometry. Generally, ϵ_s and ϵ_0 are free parameters. However, for our crystals it turned out to be a fairly good approximation to keep them equal to unity – corresponding to black-body radiation – as will be discussed later. Besides determining κ, this method also provides the steady-state temperature profile along the sample which can remarkably differ from a linear distribution in the presence of radiation.

The effect of the radiative heat transfer on the thermal conductivity as a function of temperature and the dimensionless surface aspect ratio (S/A) is demonstrated in Figure 2 using the typical values of $\kappa_0 = 4\text{W/Km}$ and $\Delta T_s = 0.5$ K for the thermal conductivity and for the total temperature drop, respectively, for the samples described below. High values of the S/A geometrical parameter correspond to a large surface area of efficient radiation relative to the cross section area of the convective heat flow. In this limit the radiative heat loss is expected to be considerable, especially at high temperatures. The horizontal lines in the figure indicate the S/A values of the three different crystals, namely BaVS_3, $2H$-TaSe_2 and κ-$(\text{ET})_2\text{Cu}_2(\text{CN})_3$.

2.3 Calculation of the specific heat in presence of thermal radiation

As shown previously, the thermal conductivity can be calculated from the experimentally determined steady-state value of ΔT_s by using equation (3). On the other hand, for the evaluation of the specific heat the time dependent $\Delta T_s(t)$ has to be monitored during the experiment. This time dependence can be reproduced by the adequate choice of c in equations (1–2). For the numerical approach, the time scale is also divided into discrete intervals as

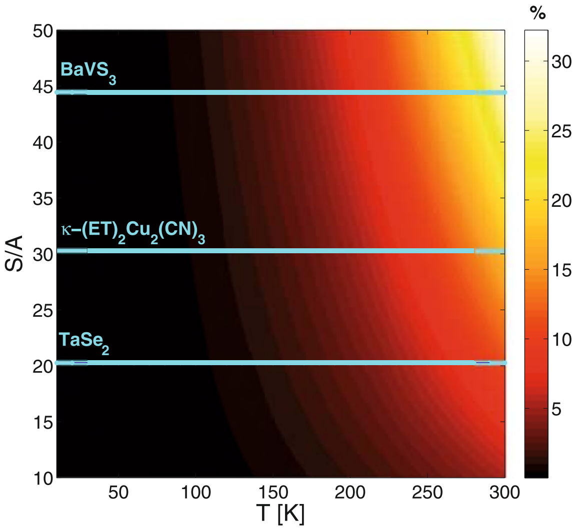

Fig. 2. (Color online) Color map of the relative error in the thermal conductivity arising from radiative heat loss and the corrected thermal conductivity value over the temperature-surface aspect ratio (S/A) plane. Horizontal lines represent the typical S/A values for the measured samples, see text for details. Values on the color scale refer to percentages.

$t = j\Delta t$. The actual temperature of the ith segment can be calculated recursively from the earlier values according to

$$T_i(t) \triangleq T_{i,j} = T_{i,j-1} + \dot{T}_{i,j-1}\Delta t. \tag{4}$$

This process is started with the initial set $\{T_{i,0}\}$ corresponding either to a uniform temperature distribution of the sample or to the steady-state profile obtained from the calculation of κ by equation (3). As a next step, the $\{\dot{T}_{i,0}\}$ values are calculated by using equations (1–2). Finally, equation (4) yields to the $\{T_{i,1}\}$ set. Similarly, the time evolution of each segment i.e., the full set of $\{T_{i,j}\}$ can be obtained recursively. At this point, for the calculation of the specific heat we only use the $\Delta T_s(t) \equiv T_N(t) - T_0$ values. The agreement with the experimentally observed time dependence of ΔT_s is checked at the end of the recursive process by means of a least-square fitting: the value of c is optimized iteratively for the minimal deviation between the calculated and experimental curves. (Since κ is fully determined by the steady-state conditions, it is not modified during these iterations.) In the absence of radiative heat loss, after turning the heater instantaneously on or off the thermal relaxation can be well approximated by the exponential form of $\Delta T_s(t) - \Delta T_s(0) \propto \exp[-t(v/L^2)(\kappa/c)]$. Although it does not give a satisfactory description in the present case, we used this fitting to determine the initial value of c for the iteration process.

In the actual calculations the sample was divided into $N = 10\ldots100$ parts while for the time discretization $\Delta t = 10^{-3}\ldots10^{-4}\tau$ was used where τ is the characteristic time scale of the relaxation. With these choices the error due to the discretization was found to be less than 1%. While the typical values of τ are in the range of a few seconds at low temperatures ($T < 10\,\mathrm{K}$), they can grow to several minutes due to the enhanced heat capacities of the samples at room temperature. In the latter case the relaxation is sufficiently slow and the standard method of data acquisition can be used. On the other hand, an increased read-out rate of the instruments is required at low temperatures realized, for example, by buffering the collected data first and recalling them in a next step.

So far we have stressed that the thermal conductivity is best determined from the steady-state equation and the dynamics is only used for the calculation of the specific heat. Note that in this case the calculated value of the specific heat is not independent from the value of the thermal conductivity, i.e. inaccurate determination of the latter also affects the former. However, at elevated temperatures the thermal relaxation can slow down so much that the approach of the steady-state would require extremely long measurement cycles. Under these conditions it is feasible to obtain both κ and c by the iterative fitting of the time dependence proposed for deducing the heat capacity.

2.4 Geometrical correction and emissivity

Measurement of the geometrical parameters for single-crystal samples with arbitrary shape can be carried out only with large uncertainty. We describe a further improvement of the experimental method by which this error can be efficiently reduced and also the effect of radiative loss can be directly checked. We placed an additional thermocouple to the middle of the specimen in order to monitor the temperature profile along the sample by measuring the temperature drop in both parts of the sample independently (see Fig. 1b).

Figure 3 shows the temperature drop in the two parts relative to the total temperature difference for the BaVS$_3$ (upper panel) and 2H-TaSe$_2$ (lower panel) crystals. At low temperatures, where the radiation is negligible, the temperature increases from the cold towards the hot end linearly in a steady-state. Therefore, in the $T \to 0$ limit the difference between $\Delta T_c/\Delta T_s$ and $\Delta T_h/\Delta T_s$ indicates that the additional thermocouple is not placed precisely in the middle of the crystal (or the cross section changes along the length) but it divides the sample proportionally to $\Delta T_c/\Delta T_h$. However, this ratio varies with increasing temperature as the temperature profile along the sample is no longer linear owing to radiative heat loss. The method described for the evaluation of κ (based on Eq. (3) using ΔT_s and the geometrical factors as input parameters) provides a complete temperature profile along the sample. Since the position of the additional thermocouple is unambiguously determined at low temperature, comparison of the temperature profile with the measured ΔT_c and ΔT_h values becomes possible at any temperatures. This is exemplified for BaVS$_3$ by the black curves in Figure 3. If the agreement with $\Delta T_c(T)$ and $\Delta T_h(T)$ is not satisfactory, the geometrical factors A, L and p can be re-adjusted and the evaluation of κ with the new parameter set has to be performed repetitively until the temperature profile is reasonably reproduced by approximating the real geometry of the crystal.

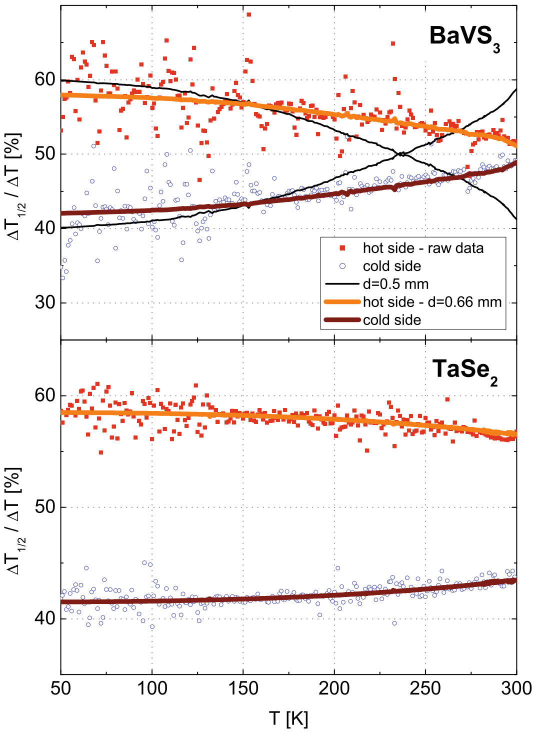

Fig. 3. (Color online) Temperature drop along the two halves of the samples for BaVS$_3$ and $2H$-TaSe$_2$. $\Delta T_c(T)/\Delta T_h(T)$ correspond to the cold/hot part (measured in the three-thermocouple arrangement) plotted by open/closed circles, respectively. For BaVS$_3$, thin and thick lines show the values evaluated before and after the geometrical correction. See text for details.

The rod-shaped BaVS$_3$ sample exhibiting a hexagonal cross-section was treated as a cylinder with a diameter of $d = 0.5$ mm predetermined with an optical microscope. However, using this value the calculated $\Delta T_c(T)$ and $\Delta T_h(T)$ lines strongly deviate from the experimental data, especially at high temperature. After fine-tuning the diameter in the iterative process described for κ, a good agreement was obtained between thick lines and the experimental data points shown in Figure 3 at a corresponding sample diameter value of 0.66 mm. In the upper panel of Figuer 4 the temperature dependence of κ is shown in the three stages of the evaluation: (i) without and (ii) with taking the effect of radiative loss into account and (iii) after precise tuning of the geometrical parameters. It is clearly visible that both type of corrections are relevant for the magnitude and the temperature dependence of κ. The same procedure resulted in $\sim$10$-$30% corrections for the other two samples.

Using the sample emissivity value of $\epsilon_s = 1$ was sufficient for the data evaluation of all the measured crystals. However, there are cases when the temperature profile of the sample cannot be well reproduced solely by the adjustment of the geometrical parameters. This applies to crystals deviating from the ideal black body behavior and hence exhibiting an emissivity of less than unity. In these cases ϵ_s should also be included among the least-square fit parameters. We studied the emissivity of Inox (as a reference material) by this approach and obtained $\epsilon_s = 0.4 \pm 0.1$ in a good agreement with the typical technical data.

3 Results and discussion

3.1 BaVS$_3$

BaVS$_3$ has a quasi-one-dimensional crystal structure formed by face sharing VS$_3$ octahedra chains along the crystallographic c-axis with $3d^1$ electron configuration on the vanadium ions. The t_{2g} subspace of the V($3d$) shell is partly occupied by itinerant electrons on the $a_{1g}(t_{2g})$ orbitals and quasi-localized electrons on the $e_g(t_{2g})$ levels [13,14]. The magnetic and transport properties of the material are expected to be extremely sensitive to the precise balance of the two types of carriers [15,16]. Beside previous electric transport, magnetization and spectroscopic studies, high-resolution specific heat and thermal conductivity measurements can give further insight into the nature of the electronic states and the dominant scattering mechanism. With lowering the temperature, BaVS$_3$ undergoes three continuous phase transitions; a second-order structural (hexagonal-to-orthorhombic) phase transition at $T_S \sim 250$ K [17] followed by a metal-to-insulator transition (MIT) accompanied by a structural tetramerization [18] at $T_{MI} \sim 69$ K. The onset of a long range magnetic order takes place at $T_X \sim 30$ K in the form of an incommensurable antiferromagnetic ordering [19]. Our study shows that both the high temperature structural and the MIT is accompanied with anomalies in the specific heat, while the thermal conductivity only indicates the onset of the MIT (see Fig. 4).

In the low-temperature insulating phase of BaVS$_3$, the thermal conductivity is dominated by the so-called phonon peak (located typically at $T \approx \Theta_D/10$) resulting from the interplay between the increasing phonon population and the enhanced phonon-phonon scattering towards high temperatures. A cusp at $T \approx 69$ K clearly indicates the onset of the insulator to metal transition. The enhancement of κ in the metallic phase is likely to have an electronic origin. In the immediate vicinity of the transition, the thermal conductivity curve exhibits a tiny peak (see inset of the upper panel in Fig. 4) interpreted in terms of fluctuations characteristic to Peierls transitions [21–23]. Note that the absolute noise level is below 10 mW/Km over the entire investigated temperature regime.

The specific heat data obtained for BaVS$_3$ are presented in the lower panel of Figure 4 in comparison with earlier results (open circles) obtained on powder samples by Imai et al. [20] Because of its fundamental thermodynamical nature, specific heat is often a more sensitive indicator of phase transitions than transport properties. In our study, owing to the high-quality single crystal sample and the improved experimental resolution, a tiny anomaly associated with the structural transition can be discerned. Furthermore, the peak at the insulator to metal transition is sharper and enlarged in magnitude as compared to the former results. The increasing difference between the

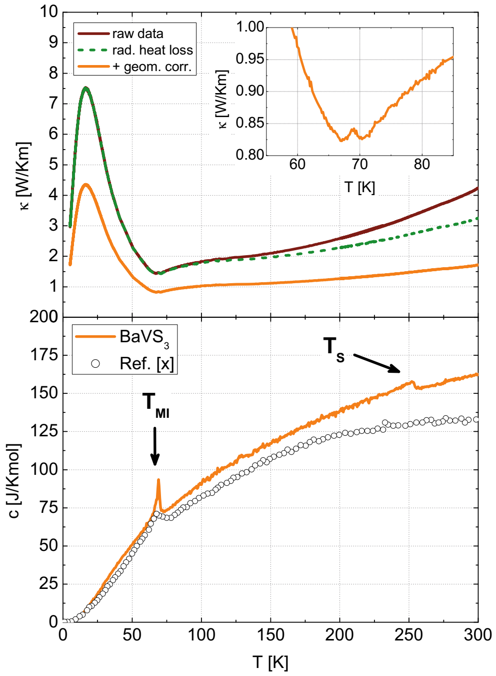

Fig. 4. (Color online) Upper panel: thermal conductivity of $BaVS_3$. Data without/with considering the effect of radiative heat loss (upper solid line/dashed line) and final data when the geometric correction has also been taken into account (lower solid line). Inset: anomaly in the close vicinity of the phase transition. Lower panel: specific heat of $BaVS_3$. Open circles represent former results adopted from Imai et al. [20] Besides the insulator to metal transition, the present study also reveals a contribution associated with the structural transition at T_S.

two curves toward room temperature is likely caused by the effect of radiation not considered in the former study. (These results will be discussed in details in a separate paper). The accuracy of the measurement is better than 2 J/Kmol at any temperatures.

3.2 $TaSe_2$

The transition-metal dichalcogenide $2H$-$TaSe_2$ has a quasi-two-dimensional lattice structure and exhibits two charge density wave (CDW) phase transitions, a second-order one at $T_{\rm NIC} \sim 120$ K from a semi-metal to an incommensurate CDW state and a first-order lock-in transition at $\sim$90 K from the incommensurate to a commensurate CDW phase [24,25]. Though the presence of these transitions has been reported three decades ago the detailed microscopic picture is still under debate. Among the thermal properties, we found that both transitions can be discerned in the $\kappa(T)$ curve, while the specific heat shows a pronounced structure at $T_{\rm NIC}$ (see Fig. 5). The critical temperature of the second-order transition is in good agreement with the previous results of Craven at al. [28] The difference in the magnitude of the specific heat data between the two experiments (about 50%) is possibly due to the uncertainty of the sample geometry in the former study.

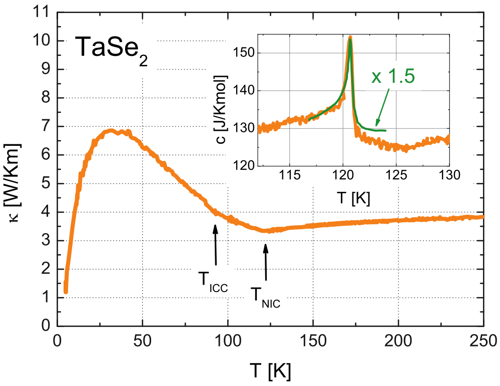

Fig. 5. (Color online) Temperature dependence of the thermal properties of $2H$-$TaSe_2$ as followed in the thermal conductivity across the two CDW transitions at $T_{\rm NIC} \approx 120$ K and $T_{\rm ICC} \approx 90$ K (main panel) and in the specific heat in the vicinity of $T_{\rm NIC}$ (inset). For comparison, specific heat data close to $T_{\rm NIC}$ adopted from reference [28] are also plotted after multiplying by a factor of 1.5 (see text for details).

The CDW transition at $T_{\rm NIC}$ appears as a dip in the thermal conductivity and as a sharp peak in the specific heat curve in good agreement with previous results [26–28]. Below $T_{\rm NIC}$ the thermal conductivity tends to increase as a result of the CDW ordering i.e., the reduced scattering rate both for phonons and electrons. Upon the second transition the $\kappa(T)$ curve shows a kink followed by a further enhancement corresponding to the phonon peak below which it starts falling proportionally to $\sim T^3$. The accuracy of the data acquisition is similar to the one obtained for $BaVS_3$.

3.3 κ-$(ET)_2Cu_2(CN)_3$

κ-$(ET)_2Cu_2(CN)_3$ is believed to be a triangular-lattice Mott insulator [29]. ET molecules are strongly dimerized [30] and the valence of the dimers is +1 i.e., the conduction band is effectively half-filled. Due to the on-site Coulomb repulsion, the system is a Mott insulator, although the ratio of the Coulomb interaction U and the effective bandwidth W is close to the critical value. The unusual temperature dependence of the magnetic susceptibility and the absence of a long-range magnetic order indicate a spin-liquid state in this system [29]. A hump structure in the heat capacity and a tiny anomaly in the thermal conductivity around $T = 6$ K has been interpreted recently as a possible crossover into a quantum spin liquid phase [31,32]. In Figure 6 we report only the thermal conductivity data over a broad temperature range which confirms the presence of such an anomaly.

After the initial decrease of κ below room temperature a broad minimum around 150 K is observed followed by a large and broad peak likely related to the opposite temperature dependence of the phonon population and anharmonicity. The lower edge of the phonon peak (enlarged in the inset) exhibits a shoulder-like anomaly which has been recently observed [31] and was also reported in the specific heat studies carried out by Yamashita et al. [32].

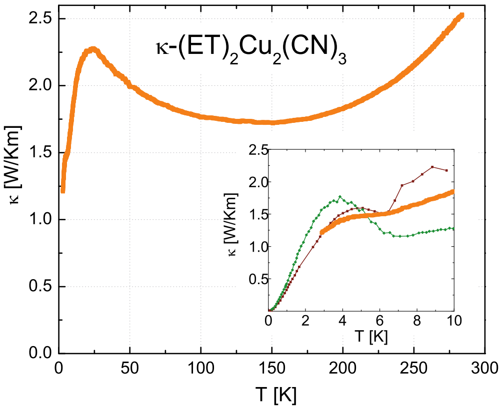

Fig. 6. (Color online). Thermal conductivity of κ-$(\mathrm{ET})_2\mathrm{Cu}_2(\mathrm{CN})_3$ in the range of $T = 3-300$ K. The inset shows $\kappa(T)$ in the low-temperature region together with data adopted from reference [31] (thin lines). Although $\kappa(T)$ is slightly sample dependent, please note that the anomaly around $T = 6$ K common for each crystal.

4 Conclusions

In conclusion, we described a method for the simultaneous, high-resolution measurement of the specific heat and thermal conductivity. Both the experimental arrangement (based on the thermal relaxation technique) and the data evaluation process have been improved in order to eliminate the systematic error arising from the radiative heat loss. In order to reduce the uncertainty in the absolute value of κ and c we also proposed a process for the accurate determination of the sample geometry using a self-consistent analysis of the experimental data. By studying three compounds – with different size, shape and thermal properties – we demonstrated that our technique is capable for the accurate determination of κ and c up to high temperatures even for small samples with arbitrary shape. The results are compared with data from the literature whenever available.

We are grateful to L. Forró, H. Berger and K. Kanoda for providing us the high-quality single crystals used in the present study. This work was supported by the Hungarian Research Funds OTKA PD75615, K62441, and Bolyai 00256/08/11. M.C. is grateful to the European Commission for financial support under a Marie Curie Intra European Fellowship.

References

1. R. Felten, F. Steglich, G. Weber, H. Rietschel, F. Gompf, B. Renker, J. Beuers, Europhys. Lett. **2**, 323 (1986)
2. K. Yano, T. Sakakibara, T. Tayama, M. Yokoyama, H. Amitsuka, Y. Homma, P. Miranović, M. Ichioka, Y. Tsutsumi, K. Machida, Phys. Rev. Lett. **100**, 017004 (2008)
3. K. Izawa, H. Yamaguchi, T. Sasaki, Y. Matsuda, Phys. Rev. Lett. **88**, 027002 (2001)
4. B. Lussier, B. Ellman, L. Taillefer, Phys. Rev. B **53**, 5145 (1995)
5. R.S. Kwok, S.E. Brown, Rev. Sci. Instrum. **61**, 809 (1989)
6. J. Hou, X. Wang, P. Vellelacheruvu, J. Guo, C. Liu, H. Cheng, J. Appl. Phys. **100**, 124314 (2006)
7. G.R. Stewart, Rev. Sci. Instrum. **54**, 1 (1982)
8. P.F. Sullivan, G. Seidel, Phys. Rev. **173**, 679 (1968)
9. J.S. Hwang, K.J. Lin, C. Tien, Rev. Sci. Instrum. **68**, 94 (1996)
10. L. Lu, W. Yi, D.L. Zhang, Rev. Sci. Instrum. **72**, 2996 (2001)
11. F. Chen, J. Shulman, Y. Xue, G.S. Nolas, C.W. Chu, Rev. Sci. Instrum. **75**, 4578 (2004)
12. R. Bachmann, F.J. DiSalvo, T.H. Geballe, R.L. Greene, R.E. Howard, C.N. King, H.C. Kirsch, K.N. Lee, R.E. Schwall, H.U. Thomas, R.B. Zubeck, Rev. Sci. Instrum. **43**, 205 (1972)
13. I. Kézsmárki, G. Mihály, R. Gaál, N. Barišić, A. Akrap, H. Berger, L. Forró, C.C. Homes, L. Mihály, Phys. Rev. Lett. **96**, 186402 (2006)
14. Y. Narumi, K. Suga, K. Kindo, T. Yamasaki, M. Shiga, H. Nakamura, J. Phys. Soc. Jpn **76**, 013706 (2007)
15. F. Lechermann, S. Biermann, A. Georges, Phys. Rev. Lett. **94**, 166402 (2005)
16. F. Lechermann, S. Biermann, A. Georges, Phys. Rev. B **76**, 85101 (2007)
17. T. Inami, K. Ohwada, H. Kimura, M. Watanabe, Y. Noda, H. Nakamura, T. Yamasaki, M. Shiga, N. Ikeda, Y. Murakami, Phys. Rev. B **66**, 073108 (2002)
18. S. Fagot, P. Foury, S. Ravy, J.P. Pouget, G. Popov, M.V. Lobanov, M. Greenblatt, Physica B **359**, 1306 (2005)
19. H. Nakamura, T. Yamasaki, S. Giri, H. Imai, M. Shiga, K. Kojima, M. Nishi, K. Kakurai, N. Metoki, J. Phys. Soc. Jpn **69**, 2763 (2000)
20. H. Imai, H. Wada, M. Shiga, J. Phys. Soc. Jpn **65**, 3460 (1996)
21. R.S. Kwok, S.E. Brown, Phys. Rev. Lett. **63**, 895 (1989)
22. K. Maki, Phys. Rev. B **46**, 7219 (1992)
23. A. Smontara, K. Biljakovic', S.N. Artemenko, Phys. Rev. B **48**, 4329 (1993)
24. D.E. Moncton, J.D. Axe, F.J. DiSalvo, Phys. Rev. B **16**, 801 (1977)
25. I. Kézsmárki, R. Gaál, C.C. Homes, B. Sípos, H. Berger, S. Bordács, G. Mihály, L. Forró, Phys. Rev. B **76**, 205114 (2007)
26. M.D. Nunez-Regueiro, J.M. Lopez-Castillo, C. Ayache, Phys. Rev. Lett. **55**, 1931 (1985)
27. M. Harper, T.H. Geballe, F.J. DiSalvo, Phys. Rev. B **15**, 2943 (1977)
28. R.A. Craven, S.F. Meyer, Phys. Rev. B **16**, 4583 (1977)
29. Y. Shimizu, K. Miyagawa, K. Kanoda, M. Maesato, G. Saito, Phys. Rev. Lett. **91**, 107001 (2003)
30. H. Kino, H. Fukuyama, J. Phys. Soc. Jpn **64**, 2726 (1995)
31. M. Yamashita, N. Nakata, Y. Kasahara, T. Sasaki, N. Yoneyama, N. Kobayashi, S. Fujimoto, T. Shibauchi, Y. Matsuda, Nature Phys. **5**, 44 (2009)
32. S. Yamashita, Y. Nakazawa, M. Oguni, Y. Oshima, H. Nojiri, Y. Shimizu, K. Miyagawa, K. Kanoda, Nature Phys. **4**, 459 (2008)